PNAS Nexus

PNAS Nexus, 2022, **1**, 1–8
https://doi.org/10.1093/pnasnexus/pgac127
Advance access publication date: 25 July 2022
Research Report

Vibrational and electrochemical studies of pectin—a candidate towards environmental friendly lithium-ion battery development

Phillip M. Wu [a,b,*,1], Ching Yi Chung[a,c,d,1], Yan Ruei Chen[a,c,d,1], Yu Hsuan Su[a,c,d], Kuei Shu Chang-Liao [d], Po Wei Chi[a], Tanmoy Paul[a], Yun Ju Chen[a], Yeng Long Chen[a], Sea Fue Wang[b], Pooja Badgujar[e], Bo-Nian Chen[e], Chia Liang Cheng[e] and Maw Kuen Wu [a]

[a]Institute of Physics, Academia Sinica, 128, Section 2, Academia Road, Taipei 11529, Taiwan
[b]Department of Materials and Mineral Resources Engineering, National Taipei University of Technology (TAIPEI TECH), 1, Sec. 3, Zhong-Xiao E. Rd., Taipei 10608, Taiwan
[c]Nano Science and Technology Program, Taiwan International Graduate Program, Academia Sinica, 128, Section 2, Academia Road, Taipei 11529, Taiwan
[d]Department of Engineering and System Science, National Tsing Hua University, 101, Section 2, Kuang-Fu Road, Hsinchu 30013, Taiwan
[e]Department of Physics, National Dong Hwa University, 1, Section 2, Da Hsueh Road, Shoufeng, Hualien 97401, Taiwan
*To whom correspondence should be addressed: Email: pmwu@gate.sinica.edu.tw
Edited By: Yi-Jun Xu

Abstract

Pectin polymers are considered for lithium-ion battery electrodes. To understand the performance of pectin as an applied buffer layer, the electrical, magnetic, and optical properties of pectin films are investigated. This work describes a methodology for creating pectin films, including both pristine pectin and Fe-doped pectin, which are optically translucent, and explores their potential for lithium-ion battery application. The transmission response is found extended in optimally Fe-doped pectin, and prominent modes for cation bonding are identified. Fe doping enhances the conductivity observed in electrochemical impedance spectroscopy, and from the magnetic response of pectin evidence for Fe^{3+} is identified. The Li-ion half-cell prepared with pectin as binder for anode materials such as graphite shows stable charge capacity over long cycle life, and with slightly higher specific capacity compare with the cell prepared using polyvinylidene fluoride (PVDF) as binder. A novel enhanced charging specific capacity at a high C-rate is observed in cells with pectin binder, suggesting that within a certain rate (∼5 C), pectin has higher capacity at faster charge rates. The pectin system is found as a viable base material for organic–inorganic synthesis studies.

Keywords: polymer-based lithium batteries, binder, chemical modifications, battery, pectin

Significance Statement:

Pectin is a natural polysaccharide material largely present in the cell walls of plants. Due to their biodegradable and nontoxic nature pectin, which is suitable for environmental friendly recycle processes, has emerged as an attractive material for Li-ion battery application. When placed in electrode, it improves the material elastic properties, material inclusion and fundamentally affects the transport mechanisms. Combining Fe in pectin improves the capacity and maintains fast charging performance.

Introduction

The demand of energy storage devices for applications in mobile device, electric vehicle, and large-scale energy storage system makes Li-ion battery (LIB) indispensable because it is compact, relatively stable, and high energy dense. Considering worldwide market growth rate and the average life of LIBs, which is about typical 5∼10 y, one immediately foresees the problems of serious price fluctuation in raw materials for LIBs productions and the environmental impacts from the disposal of spent LIBs. The development of LIBs manufacturing processes following the circular economy framework could potentially bring a sustainable solution where waste components can be reused in the manufacturing cycle (1, 2). Many reports indicated that using regenerated material as replacement, manufacturing cost can be kept at a relatively constant level and recycling of LIBs can effectively reduce energy consumption and carbon footprint (3–6).

However, there exists a critical issue in the current recycling processes. In particular, the use of the calcination process on the current LIBs, which commonly use polyvinylidene fluoride (PVDF) as binders for electrodes, the negative electrode at least. The calcination process on PVDF is known to cause the expulsion of potentially unhealthy incineration gases, unwanted compounds such as HCN, HF, CH_4, HCHO, COF_2, SiF_4, HNCO, higher hydrocarbons, nitrogen oxides, CO, and

Competing Interests: The authors declare no competing interests.
[1]P.M.W., C.Y.C., and Y.R.C. contributed equally to this work.
Received: February 9, 2022. **Accepted:** July 20, 2022

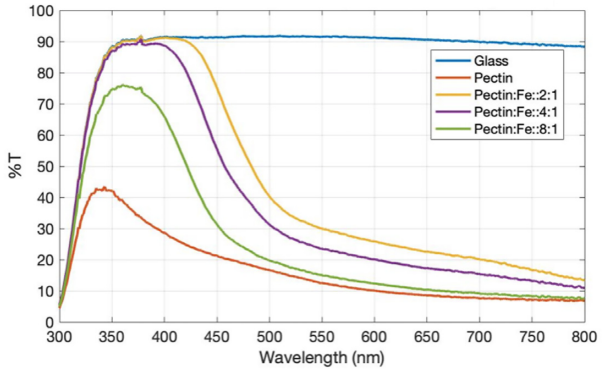

Fig. 1. Ultraviolet-visible response of the pectin thin film with and without iron doping.

CO_2, among others (7). These byproducts are produced when electrodes are incinerated in air and must not be released to the environment.

Therefore, it is strongly desirable to find an environmentally friendly binder materials to replace PVDF for LIBs. Polysaccharide polymer binders such as alginate and carboxymethyl cellulose are possible replacement materials (8, 9, 10). Among the natural materials investigated, pectin is a naturally available polysaccharide material that is largely present in the cell walls of plants. Different citrus products like apple, pomace, and oranges under mildly acidic conditions can be used to extract pectin (11, 12). Due to their biodegradable and nontoxic nature pectin has emerged as an attractive material for LIBs application and is the focus of this work.

The poly-galacturonic acid (PGA) extracted from different plants have varying degree of methoxylation (DM). High DM denotes PGA with greater than 50% of all monomers having methylester side groups, and low DM denotes less than 50% of all monomers being acidic side groups. High DM pectin networks are cross-linked by hydrogen bonds, while low DM pectin networks are cross-linked by multivalent ions such as calcium. In low DM pectin gels, consecutive PGA–calcium bonds form junction zones to stabilize the cross-links and are critical for network formation. The different structure and types of cross-link, such as the critical junction zones in low DM PGA–calcium bonds (13–18), affect the physical properties of the polymer such as the magnetic structure, optical and conductive response.

Interests in pectin arise from its potential as an applied buffer layer that can be inserted into crystal structures during the lithiation process (19, 20). Pectin when placed in electrode materials may improve the material elastic properties, featuring frequency dependent storage and loss moduli. Initial gels have longer mesh links while mature gels exhibit submicron mesh sizes (12). Detailed characterizations of pectin's optical, magnetic, and electrochemical properties, both the pristine and Fe-doped materials (11–14, 21–23), are investigated for lithium batteries performance.

Results and discussion

Figure 1 displays the ultraviolet-visible response of the pectin-Fe material, after subtraction of a glass background. The raw data optical response is shown as Figure S1. The pristine pectin sample is a translucent (orange) material. Addition of iron in 2:1 :: pectin:iron ratio optimally extends the transmission response above 400 nm. Pectin band energies obtained from these measurements are nearly 3 eV, and are lowered with addition of iron.

Table 1. Wavenumber positions and their assignment of bands and modes observed in the Raman spectrum and Fourier transform infrared spectroscopy (FTIR) from the samples, Pectin, Pectin–Fe 2:1, Pectin–Fe 4:1, and Pectin–Fe 8:1.

IR assignment (cm^{-1})		Raman assignment head 4	
Wavenumber (cm^{-1})	Assignment	Wavenumber (cm^{-1})	Assignment
884	CH_3	331, 333	330- Pectin dominant bands
993	CH_3	441, 444	443- Pectin dominant bands
1,019	Si–O	852, 854	855 (COC) Skeletal of alpha-anomers, Pectin standard Raman bands
1,094	C–O	1,755	1750 υ(C=O) ester, Pectin C–H stretching band
1,150	C–O	2,943, 2,949	
1,240	Amide III		
1,300	CH_3		
1,460	CH_3		
1,632	O–H		
1,739	C=0		
2,960	C–H		

These observations are consistent with the results of impedance measurements. The increasing transmission in Fe-added samples in UV-VIS spectra is probably related with the conformation of the molecule in the structure.

The peak assignments from the Raman and infrared (IR) observations are listed in Table 1. The pectin molecule in cell walls is primarily a galacturonan (11). The galacturonan molecule is generally a linear chain of alpha-1, 4-D-galacturonic acid units with some of the hydrogen sites replaced by for example methanol or acetyl groups (12, 24). In different fruits, the galacturonan backbone can be hundreds of galacturonic acid residues in length. DM is defined as a ratio of methyl-esterified carboxyl groups versus the total amount of galacturonic acid units and is found by calculating the areas under the peaks at 1600–1630 and 1740 cm^{-1}. Using the calibration curve, we were able to obtain the methyl esterification degree (MED) (25) of the pectin-Fe samples to be: Pectin (77.7%), Pectin–Fe (8:1, 37%; 4:1, 33%; 2:1, 12%).

In the pectin-iron samples prepared for this study, broad features at 1600–1630 and 1740 cm^{-1} are identified as OH and C=O stretches, respectively, in the Fourier transform infrared spectroscopy measurements, as shown in Figure 2. The Raman spectra bands for pectin is usually at 2,948, 1,750, 850, 817, and 479 cm^{-1}, as shown in Figure 3. From the pectin film, we clearly observed dominant band of pectin at 331, 333, 441, 444, 852, and 854 cm^{-1}. The observed spectral band at 1,755 corresponds to υ(C=O) ester, and the bands at 2,943, 2,949 cm^{-1} are the C–H stretching bands. As observed in our measurements, the bands at 854 and 852 cm^{-1} corresponds to the band for (COC) skeletal mode of α-anomers in pectin and is also considered the standard Raman band for pectin molecule (26, 27). Also, the sharp band at 854 cm^{-1} is considered as the marker band for α-glycosidic bonds in pectin, which is highly sensitive to the o-acetylation in pectin (28). The Raman bands originating from 2,949 cm^{-1}, as observed in pectin–Fe 2:1, and 4:1, are the Raman band assigned to originally 2948 υ(CH) (27). Also, the Raman spectral band from 850 to 862 cm^{-1} is highly dependent on the increasing degree of pectin acetylation (27). The Raman bands at 2,943, and 2,949 cm^{-1} are also strongly observed in pectin–Fe 2:1, 4:1 samples, which are assigned to the C–H band.

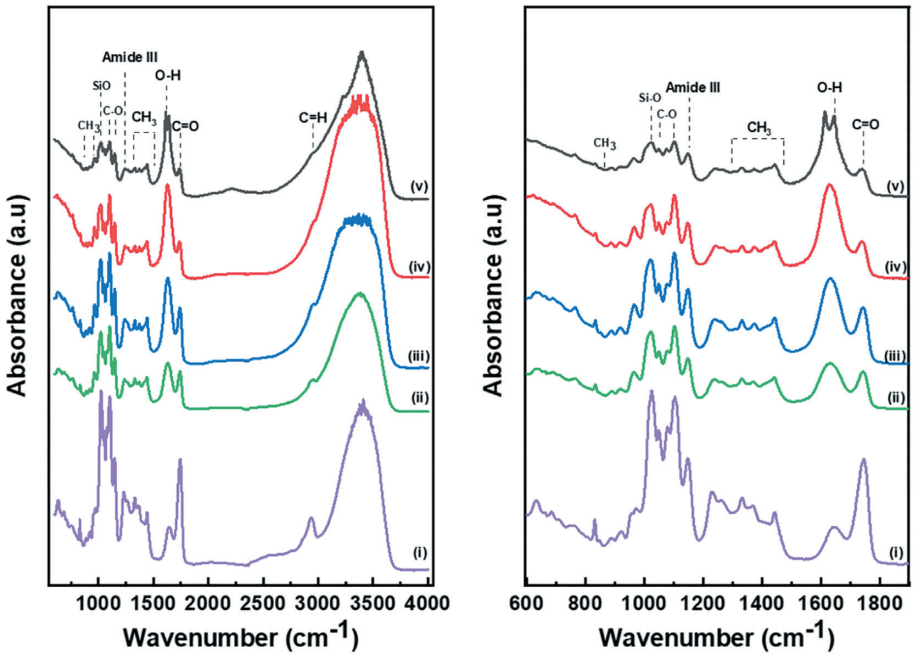

Fig. 2. The FTIR spectra of (i) Pectin, (ii) Pectin–Fe 8:1, (iii) Pectin–Fe 4:1, (iv) Pectin–Fe 2:1, and (v) Pectin–Fe 1:1 measured in air. The FTIR spectra were measured from the range 600 to 4,000 cm^{-1} (left). The expanded range from 595 to 2,000 cm^{-1} are shown (right).

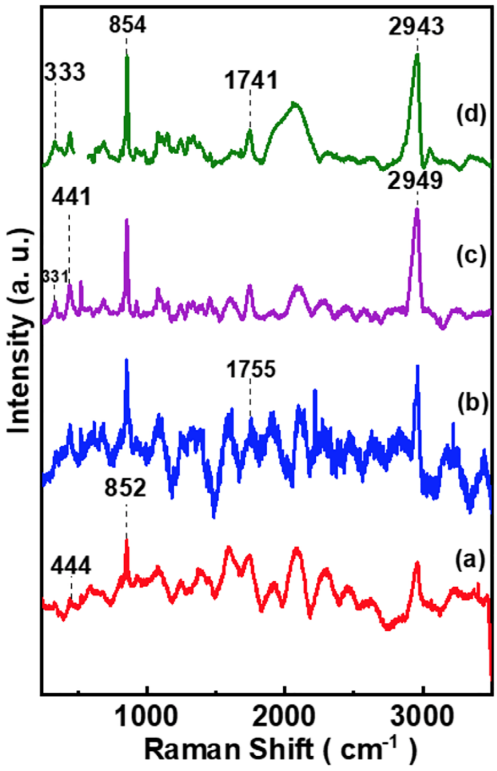

Fig. 3. The Raman spectra of pectin with different Fe-doped concentrations: (a) Pectin (film), (b) Pectin–Fe 8:1 (film), (c) Pectin–Fe 4:1 (film), and (d) Pectin 2:1.

It is known from the literature that the C–H stretching band is shifted from 2,943 for highly methylated pectin to around 2,895 cm^{-1} for cellulose and xyloglucan. As the concentration of pectin increases in the sample, we observed the Raman band at 1,755 cm^{-1} in pectin–Fe 8:1, which corresponds to 1,750 υ(C=O) ester carbonyl group, and the spectral bands around 1,750 cm^{-1} are the stretching vibrations used to distinguish pectin with different esterification degree (29). The Raman bands at 1,454 and 1,455 cm^{-1} can be assigned to the hemicellulose (xyloglucan) bands in plant cell wall polysaccharides (29). The dominant peaks for pectin were intensely observed in pectin, pectin–Fe 2:1, 4:1, and 8:1. Raman measurements identify peak features in the range 1,200 to 1,600 cm^{-1} that could be associated with increasing iron content in the pectin:Fe samples as ratio is increased from 8:1 to 2:1. These peaks suggest that bonding is occurring in the pectin:Fe, and at CH, COH, and COO- sites. These modifications, such as at the C=O bonds, affect the light transmission.

Figure S2 shows the solid state magnetic susceptibilities for pectin:iron-doped samples measured with a superconducting quantum interference device (SQUID) magnetometer. These measurements indicate that iron is included in the sample after doping, and the pristine pectin is the combination of weak paramagnet and diamagnet so that the magnetic susceptibility exhibits a diamagnetic drop at about 230 K and sharp-rise at low temperature. The magnetic susceptibility for the pristine pectin is in the order of 10^{-6} emu/Oe*g, consistent with the SEM-EDX result, indicating the presence of Ca-ion that contributes to the paramagnetic-response. The diamagnetic component may originate from the in-plane CH_3 pyranoid ring that couples with Ca-ion.

The increase in Fe-content clearly suppresses the diamagnetic component and the sample with highest Fe-content becomes paramagnetic. In the 2:1 sample, the effective magnetic moment of 5.85 μ_B (Bohr magneton) is very close to the theoretical magnetic moment of Fe^{3+}, though it is known that Fe^{2+} in different paramagnetic molecular matrix show magnetic moment can be in the range of 4.9 to 6.7 μ_B. Magnetic response consistently show that the pristine pectin contains both a weak diamagnetic component, which appears as a weak diamagnetic loop at low field and paramagnetic contribution with linear magnetization-field response in high field regime.

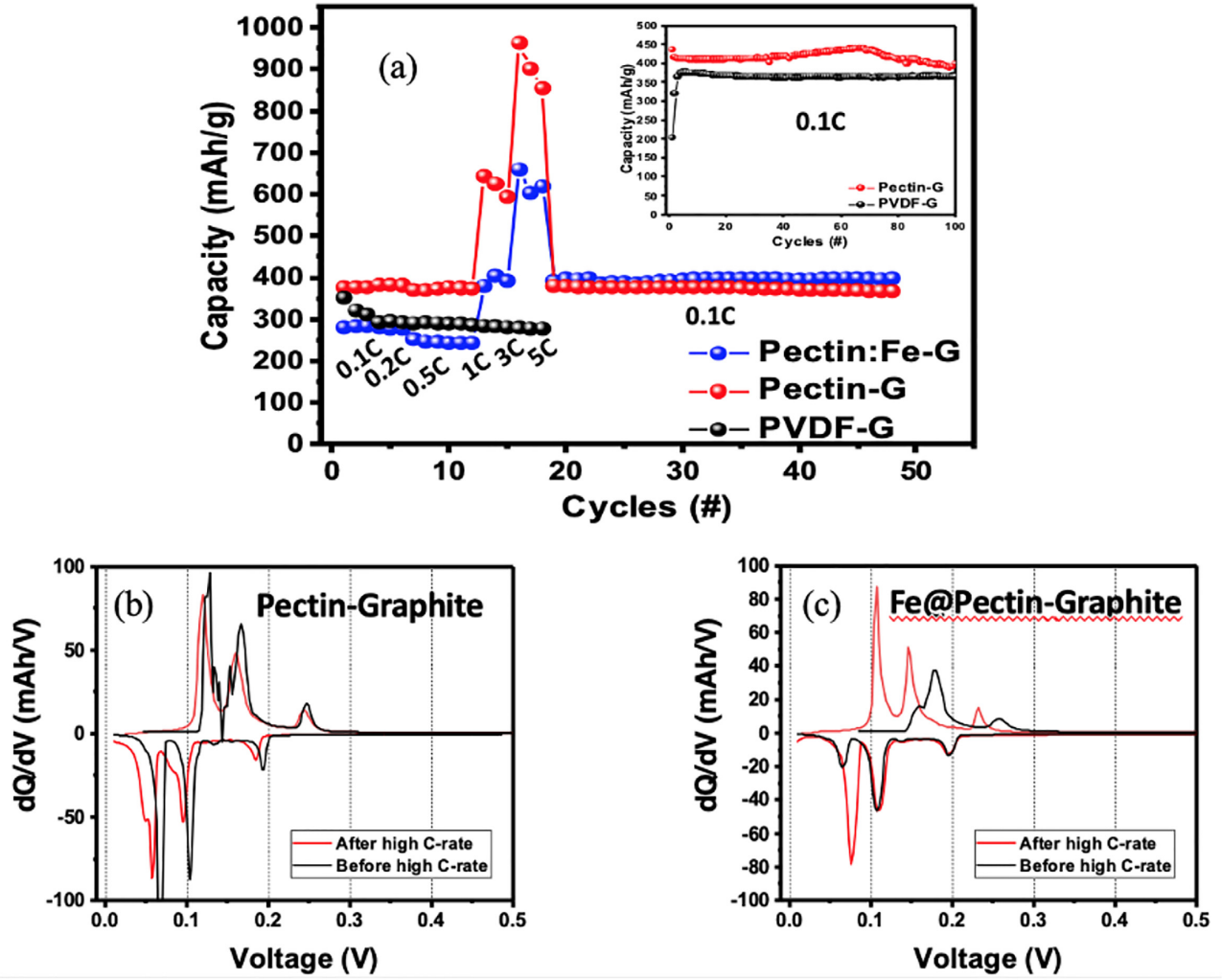

Fig. 4. Charge/discharge processes for pectin as binder. (a) Specific capacities at different C-rate for graphite with PVDF, pectin and pectin:Fe binder. The inset is the long cycle test for PVDF and pectin binders. dQ/dV versus voltage of graphite-pectin (b) and graphite-Fe–doped pectin (c).

The egg box model may still apply in describing the material response, with iron bonding instead of calcium, which is also consistent with FTIR and Raman results (30–33). It is noted that a preliminary 3-D nano-tomography (using X-ray phase contrast technique) of iron-doped pectin from Taiwan National Synchrotron Radiation Research Center show that the doped Fe-ions locate uniformly in the pectin particle.

The lithiation–delithiation electrochemistry of PVDF-graphite, pectin-graphite, and pectin:Fe-graphite are compared in Figure S3a to c. The performance of PVDF and pectin are comparable when countered with graphite. Addition of iron in graphite pectin mixture shows two peak reactions processes, as shown in Figure S3(c). The peak at 1.6 V has been observed in α-$LiFeO_2$ anode based Li-ion battery (22, 23), which is consistent with the Fe^{3+} state in pectin:Fe by magnetic measurements.

Figure 4(a) displays the cycling performance of graphite with PVDF, pectin and pectin:Fe binder, including capacity at different C-rate. The capacity maintains stable up to 100 cycles for both pectin-graphite and PVDF-graphite, in Figure 4(a) inset, indicating the good stability of the pectin material.

Specific capacity for PVDF-graphite anode is stable at 360 mAh g^{-1}. However, this value is much lower than the maximum value of 435 mAh g^{-1} observed for pectic-graphite in Figure 4. Though the specific capacity of pectin-graphite decreases after reaching maximum at 68 cycles, its value maintains around 400 mAh g^{-1} at long cycle, which is higher than that of PVDF-graphite, consistent with expectation that pectin has better elastic property than PVDF (34). A large elastic property is more beneficial to anodes experiencing large volume changes during cycling. Therefore, the reason behind the capacity increment can be attributed to the high strain resistance in pectin as well as strong affinity to bonding with the active material surface, leading to remarkable cycling performance of the graphite electrode (35). In sum, good binding property can efficiently enhance lithium-ion transport, which is evident from Figure 4.

The effect of the binders is examined at different charge/second C-rates (0.1 to 5 C) as shown in Figure 4 (a). The C-rate characterization of half-cell was performed between 3 and 0.01 V versus Li/Li^+, and all lithiation was performed at 0.1 C, then delithiation changed at 0.1, 0.2, 0.5, 1, 3, and 5 C (36). For the pectin-based electrode, a steady capacity retention is observed up to 1 C indicating the applicability of pectin as binder. Interestingly, capacity increases dramatically at high rate of 3 C in pectin-based electrodes. Conversely, the C-rate for PVDF-graphite is conventional, decreasing with increasing C-rate.

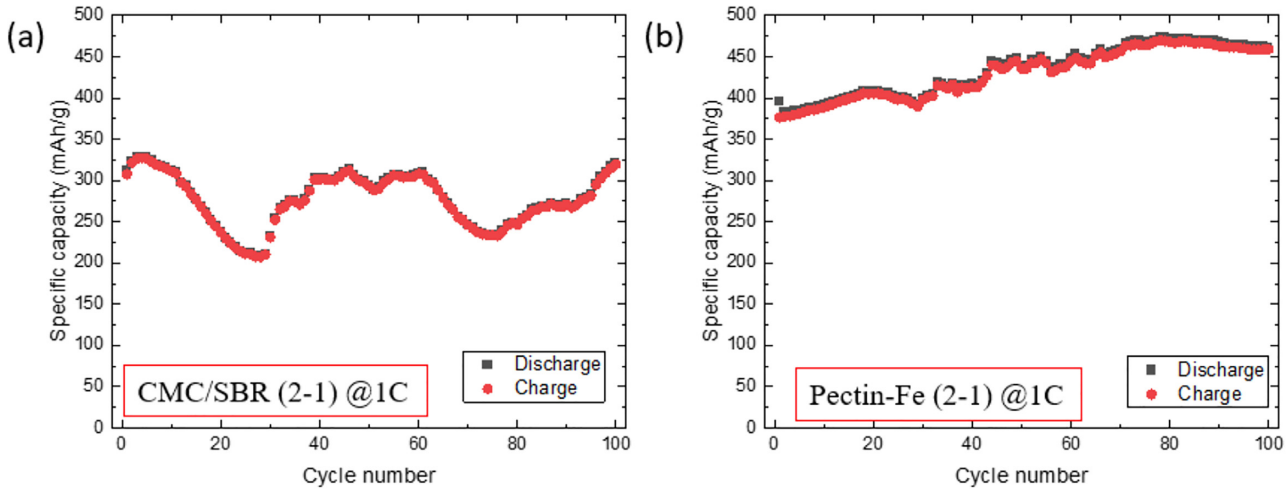

Fig. 5. Cycle performance of the (a) natural graphite electrode made with CMC/SBR binder and (b) natural graphite electrode made with Pectin-Fe binder at 1 C rate.

Similar anomalous C-rate performance with a presumed capacity switching at 3 C is also observed in pectin:Fe binder for graphite anode. However, the initial specific charging capacity in pectin:Fe binder is lower in value in comparison with the pristine pectin binder at 0.1 C. When the measurement resets to 0.1 C after high C-rate measurements, the capacity increases to a value larger than for the pristine pectin and remains the same value to longer cycles. This suggests addition of Fe to pectin indeed enhances the charge storage capability, and supports the observed Fe^{3+}-state (23) by magnetization measurement. The relatively low capacity at low initial C-rate in pectin:Fe can also be understood based on the dQ/dV analysis, shown in Figure 4 (b) and (c) for pectin and pectin:Fe, respectively. The data suggest for pectin:Fe the graphite does not contribute much to capacity initially at low C-rate before switching at 3 C.

At present, it is unclear why the switching occurs at 3 and 5 C for pectin-graphite based electrodes. However, this could be due to different activation energies of Li-ion transport at room temperature. The migration energies for Li in graphite are 0.4 eV. (37) The current–voltage results are shown in Figure S4. The current increase with increasing the applied voltage indicates that the resistance state of pectin binder switched from high to low. Defects could form trap sites below the conduction band, where the injected charge carriers (Li for instance) can be entrapped. Some trap sites may result from the chemical composition of the pectin, such as the carboxyl unit, amino linkage, and carbonyl group, acting as the nucleophilic or electrophilic sites and those defects will form conducting filament and lead to lower resistance of pectin (37–40). Possibly, an interfacial surface charge between the active material and pectin induces interfacial polarization resulting in a charge redistribution that contributes to the capacity during the charge process. Similar mechanism is also reported for SnO_2/aerogel hybrid electrode (12–14, 41–43). These results indicate pectin holds promise in fast resistive random access memory (RRAM) applications (39, 44).

We have also tested the binder performance of CMC/SBR in comparison to Fe-pectin. We choose Fe-pectin because it shows superior performance. The results are shown in Figure 5, where 5(a) displays the specific capacity of graphite using CMC/SBR (with 2:1 ratio) as binder under 1 C rate up to 100 cycles; and 5(b) is that using Fe-pectin binder. The specific capacity using CMC/SBR as binder fluctuates between 350 and 200 mAh g^{-1} in this study. The result is comparable to the reported value (10). On the other hand, the capacity of graphite using Fe-pectin as binder under 1 C rate shows an initial capacity about 350 mAh g^{-1} and gradually increases to a stable value close to 450 mAh g^{-1} at 100 cycles. Figure S5 shows the charge–discharge curves up to 10 cycles (in 1 C) of graphite using CMC/SBR (with 2:1 ratio) as binder; and that using Fe-pectin binder, respectively. It is noted that the theoretical specific capacity of natural graphite is 372 mAh g^{-1}. The result of close to 450 mAh g^{-1}, which is higher than the theoretical value for graphite, in the cell using Fe-pectin as binder is surprising. This observation suggests that the Fe-pectin may play the role to allow more Li-ion to be interacted in the active material. It is currently under further investigation to better understand this unexpected result.

Electrochemical impedance spectroscopy (EIS) coupled with the distribution of relaxation times is employed to study the ion transport for all the samples at both lithiation and delithiation conditions. Comparing Figure S6 (b), (c), (e), and (f) during lithiation and delithiation the total impedance is much lower for graphite-Fe–doped pectin sample indicating better conductivity and charge transfer mechanism. The solid lines in Figure S6 represent the fitting of the EIS data using the DRTtools package. The whole distribution of relaxation times (DRTs) contain three main peaks around 1.6 kHz, 3.2 and 0.2 Hz, (Figure 6) starting from right to left. The DRTs are found from EIS measurement, shown in Figure S6. The positions of peaks S1, S2, and S3 correspond to surface film resistance as obtained due to Li-ion migration through electrode surface, and electrode/electrolyte interfacial charge transfer resistances, respectively. Similar peaks are also detected for α-$LiFeO_2$ anode based Li-ion batteries (23). The analysis confirms the lithiation process is binder induced. The surface film effect, which occurs at OCV in pectin-graphite only, maintains a contribution till the delithiated voltage of 0.1 V. In contrast, the interfacial charge transfer effect is not observed at the lithiated and delithiated voltages of 0.01 and 0.1 V, respectively. Peak S3 is related to lithiation/delithiation of graphite and binder. More specifically, the lithiation process invokes a charge transfer process across the graphite/electrolyte interface

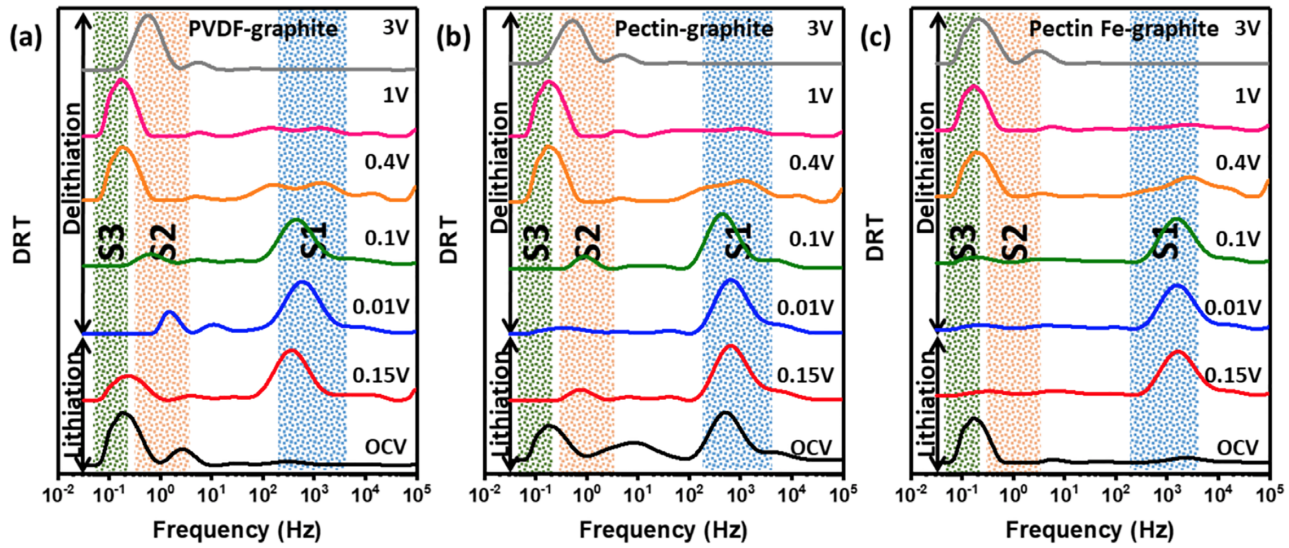

Fig. 6. DRT of graphite and binder. The binder choices are (a) PVDF, (b) pectin, and (c) pectin:Fe binder.

but the additive property of binder helps such interfacial process. The lithiation processes may have an effect for steady capacity retention [Figure 6(a)] as seen for polyacrylic acid based silicon-graphite anode (45).

The high-capacity behavior for pectin related samples can be considered as diffusion-controlled intercalation processes (DIP) or surface-induced capacitive processes (SCP) (46). For DIP, the current is linearly proportional to the square root of the voltage (V) whereas for SCP current is proportional to voltage. As the current is accumulation of total charge (Q) over time; the Q (in Figure 4) is a summation of Q_d and Q_S as obtained from DIP and SCP, respectively. Both the lithiation (1.5 to 0.1 V) and delithiation processes (0.4 to 1.5 V) are ascribed as DIP assisted for pectin:Fe-graphite, unlike PVDF-graphite and pectin-graphite samples (Figure S3) where SCP is noted. Thus, the high capacity in pectin-Fe is possibly from dominating DIP effect. The capacitance from Peak S1 for all the samples is calculated in order to determine the SCP quantitatively. Peak S1 shifts towards low frequency side for both graphite-pectin and PVDF-graphite samples but not in pectin:Fe-graphite suggesting ionic motion is transition metal dependent. As observed from Table S1, during lithiation and initial delithiation (up to 0.1 V) the peak S1 possesses lowest capacitances (~1 μF) for pectin-Fe, unlike graphite-PVDF and pectin-graphite. Overall, due to this dominating DIP and low capacitances pectin:Fe shows highest capacity among three samples. Highest columbic efficiency for pectin:Fe is observed (Figure S7), which could be due to highest number Li-ion transference per formula unit in a single charge discharge cycle. Previously, up to 11 Li-ion transfer per formula unit is reported for cubic Fe_3O_4 and Ti-doped Fe_3O_4 samples. Overall, we can confirm that the presence of Fe facilitates the charge transfer process and the electronic conductivity.

In order to assess the potential of pectin polymers for use in lithium-ion battery electrodes, we have characterized the detailed properties of Fe-doped pectin films, see Figure S8 for an SEM image. These results suggest that the interface between pectin and active materials may provide additional channel for charge storage. This is consistent with the suggestion that the material could exhibit better charge holding capacity and is suitable for supercapacitor application. These observations suggest one might be able to achieve, using the pectin-based materials, battery with both high energy and high-power density.

Experimental section/methods and materials

Magnetic data: $FeCl_2$ (with pectin:iron ratio by weight in 1:0, 2:1, 4:1, and 8:1) is mixed with deionized water and then pure pectin is added in 5% mixture aqueous solution with one day stirring. After slurry has dried, the material is taken for characterization. Magnetic susceptibility of pristine pectin and Fe-doped pectins are measured with a Quantum Design SQUID magnetometer from 300 to 2 K. For the measurement of dc magnetization (M), the magnetic field was applied in both field-cooling (FC) and zero field-cooling (ZFC) protocols. In the case of FC, the magnetic field of 3,000 Oe was applied to the samples at room temperature and measurements were performed during cooling, whereas in ZFC, the samples were cooled in a zero magnetic field, but a nonzero field was applied during the heating processes.

Half cell data: Pectin-graphite and Fe^{2+} added pectin-graphite are prepared as slurries for lithium half cells. Fe^{2+} added pectin is mixed with 5% deionized (DI) water, and stirred for 1 day. The slurries (5%) are then mixed (by weight, pectin:iron in 1:0, 2:1, 4:1, and 8:1 ratios) with graphite 90%, and carbon blacks (Super P) 5%. Mixtures are coated on copper (Cu) foils and dried at 110°C in oven. Electrode foils are punched into circular 14-mm-diameter discs for lithium half cell assembly. The electrolyte solution was prepared by adding 1 mol L^{-1} of $LiPF_6$ in a mixture of ethylene carbonate (EC) and diethyl carbonate (DEC) having a 1:1 volume ratio. A Celgard polypropylene membrane was used as a separator. The CR2032-type coin cells were assembled in an argon-filled glove box. The electrochemical properties of the samples in CR2032-type coin cells were tested at room temperature with metallic lithium as the counter electrode.

Cyclic voltammetry was performed at scan rate of 0.1 mV s^{-1} at room temperature for the CR2032-type coin cells using a PARSTAT MC 200 electrochemistry workstation between 3 and 0.01 V. The charge and discharge profiles were collected by galvanostatic cycling between 0.01 and 3 V versus Li^+/Li, applying a constant current of 0.1 C rate at room temperature with a Think Power

battery testing system. EIS was performed by the same workstation for the CR2032-type coin cells using an AC amplitude of 10 mV between 100 kHz to 0.01 Hz. From the impedance spectra measurements, the distribution function of relaxation times (DFRTs) was calculated (23, 47, 48). The DRTs are considered up to 0.1 Hz as shown in the analysis.

UV-VIS measurements: Ultraviolet visible transmission was taken with a Lambda Spectrometer in the range of 300 to 800 nm. Samples were placed on glass slide and the light transmission through glass is taken as background and subtracted from the sample data.

Raman and IR measurements: A micro-Raman spectrometer (Renishaw1000 B, UK) with a grating (1800 mm^{-1}) coupled with a microscope (Leica, Germany) was used for the Raman measurements. The samples were excited by a Diode-Pumped Solid-State laser (DPSS) that was operated at 532 nm wavelength with a laser power of 3.7 mW focused onto the sample through 50 × objective (NA = 0.75). The spectra were acquired at a spectral resolution of 0.1 cm^{-1}, with the laser spot size of about 1.5 microns, at the spectral range of 200 to 3500 cm^{-1}. The acquired Raman spectra were baselined corrected and fitted using Lorentzian fitting in the Origin software.

For the IR measurements, an FTIR (Bomem, Canada) was used. The pectin powder of 2 mg was dissolved in 200 μl double distilled water (DD water), then subject to sonication to achieve uniform dispersed solution. After complete solubility, to prepare samples for IR observation, initially 40 μl of the solution was dropped onto silicon wafer used as sample holder. After it dried, 20 μl each time until total 2 mg of pectin was deposited on the silicon wafer. The Si wafer was then placed in the light path of the FTIR, each spectrum was obtained with 400 scans acquisition using 4 cm^{-1} instrumental resolution and a deuterated triglycine sulfate (DTGS) detector.

Acknowledgment

We also acknowledge Prof. Ryan Lin at the National Taipei University of Technology for their technical support in IV measurements. The authors acknowledge Dr. Chun-Chieh Wang at the Taiwan National Synchrotron Radiation Research Center for providing the 3-D nano-tomography of iron-doped pectin taken from Beamline TLS-01B1.

Supplementary Material

Supplementary material is available at *PNAS Nexus* online.

Funding

The authors greatly appreciate the financial support from the Executive Yuan through its Forward-Looking Research Grant Number 109–0210–04–20–01. P.M.W. acknowledges the support from the MOST visiting scholar program under Grant Number 109–2811-E-027–506.

Authors' Contributions

All authors contributed to the writing and editing of the manuscript. M.K.W., Y.L.C., and P.M.W. designed study; P.M.W., C.Y.C., Y.R.C., Y.H.S., P.W.C., T.P., and Y.J.C. prepared samples and performed optics, magnetism, and battery measurements; Raman and FTIR measurements presented in the paper by P.B., B.N.C., and C.L.C., and discussed with authors; and C.L.C., S.F.W., Y.L.C., K.S.C.-L., and M.K.W. supervised work.

Data Availability

All data are included in the manuscript and/or supporting information.

References

1. Allwood JM. 2014. Chapter 30 - squaring the circular economy: the role of recycling within a hierarchy of material management strategies. In: Worrell E, Reuter MA, editors. Handbook of recycling. Amsterdam: Elsevier. p. 445–477.
2. Geissdoerfer M, Savaget P, Bocken NMP, Hultink EJ. 2017. The circular economy—a new sustainability paradigm? J Cleaner Prod. 143:757–768.
3. Li L, *et al.* 2013. Recovery of metals from spent lithium-ion batteries with organic acids as leaching reagents and environmental assessment. J Power Sources. 233:180.
4. Zhang T, *et al.* 2014. Chemical and process mineralogical characterizations of spent lithium-ion batteries: an approach by multi-analytical techniques. Waste Manage (Oxford). 34:1051.
5. Grützke M, *et al.* 2015. Extraction of lithium-ion battery electrolytes with liquid and supercritical carbon dioxide and additional solvents. RSC Adv. 5:43209–43217.
6. Grey CP, Tarascon JM. 2017. Sustainability and in-situ monitoring in battery development. Nat Mater. 16:45.
7. Hanisch C, *et al.* 2015. Recycling of lithium-ion batteries: a novel method to separate coating and foil of electrodes. J Cleaner Prod. 108:301.
8. Zhang S, *et al.* 2019. Aqueous sodium alginate as binder: dramatically improving the performance of dilithium terephthalate-based organic lithium-ion batteries. J Power Sources. 438: 227007.
9. Zhang S-J, *et al.* 2018. Sodium-alginate-based binders for lithium-rich cathode materials in lithium-ion batteries to suppress voltage and capacity fading. ChemElectroChem. 5(9):1321–1329.
10. Schlemmer W, Selinger J, Hobisch MA, Spirk S. 2021. Polysaccharides for sustainable energy storage—a review. Carbohydr Polym. 265:118063.
11. Gawkowska D, Cybulska J, Zdunek A. 2018. Structure-related gelling of pectins and linking with other natural compounds: a review. Polymers. 10(7):762.
12. Wang FW, *et al.* 2022. Rheo-chemistry of gelation in aiyu (fig) jelly. Food Hydrocoll. 123:107001.
13. Ventura I, Jammal J, Bianco-Peled H. 2013. Insights into the nanostructure of low methoxyl pectin-calcium gels. Carbohydr Polym. 97:650–658.
14. Luzio GA, Cameron RG. 2008. Demethylation of a model homogalacturonan with the salt-independent pectin methyl esterase from citrus. Part II. Structure-function analysis. Carbohydr Polym. 71:300–309.
15. Durand D, Bertrand C, Clark A, Lips A. 1990. Calcium-induced gelation of low methoxy pectin solutions—thermodynamic and rheological considerations. Int J Biol Macromol. 12:14–18.
16. Braccini I, Perez S. 2001. Molecular basis of Ca2+ induced gelation in alginates and pectins: the egg-box model revisited. Biomacromolecules. 2:1089–1096.
17. Munarin F, Tanzi MC, Petrini P. 2012. Advances in biomedical applications of pectin gels. Int J Biol Macromol. 51:681–689.
18. Suzuno H, Kinugasa S, Nakahara H, Kawabata A. 1997. Molecular characteristics of water-soluble polysaccharide extracted from jelly fig (*Ficus awkeotsang* Makino) seeds. Biosci Biotechnol Biochem. 61(9):1491–1494.

19. Lu XF, *et al.* 2013. Superconductivity in LiFeO2Fe2Se2 with anti-PbO-type spacer layers. Phys Rev B. 89:020507(R).
20. Burrard-Lucas M, *et al.* 2013. Enhancement of the superconducting transition temperature of FeSe by intercalation of a molecular spacer layer. Nat Mater. 12(1):15–19.
21. Chandan P, *et al.* 2019. Voltage fade mitigation in the cationic dominant lithium-rich NCM cathode. Commun Chem. 2: 120.
22. Su KH, *et al.* 2021. Lithiation and delithiation induced magnetic swtiching and electrochemical studies in alpha-$LiFeO_2$ based Li ion battery. Materials Today Physics. 18:100373. doi.org/10.1016/j.mtphys.2021.100373.
23. Paul T, Chi PW, Wu PM, Wu MK. 2021. Computation of distribution of relaxation times by Tikhonov regularization for Li-ion batteries: usage of L-curve method. Sci Rep. 11:12624. doi.org/10.1038/s41598-021-91871-3.
24. Morris ER, Powell MJ, Gidley MJ, Rees DA. 1982. Conformations and interactions of pectins. I. Polymorphism between gel and solid states of calcium polygalacturonate. J Mol Biol. 155:507–516.
25. Manrique GD, Lajolo FM. 2002. FT-IR spectroscopy as a tool for measuring degree of methyl esterification in pectins isolated from ripening papaya fruit. Postharvest Biol Technol. 25: 99–107.
26. Gierlinger N, Sapei L, Paris O. 2008. Insights into the chemical composition of Equisetum hyemale by high resolution Raman imaging. Planta. 227(5):969–980.
27. Chylińska M, Szymańska-Chargot M, Zdunek A. 2014. Imaging of polysaccharides in the tomato cell wall with Raman microspectroscopy. Plant Methods. 10:14.
28. Synytsya A, Čopíková J, Matějka P, Machovič V. 2003. Fourier transform Raman and infrared spectroscopy of pectins. Carbohydr Polym. 54(1):97–106.
29. Szymańska-Chargot M, *et al.* 2016. Raman imaging of changes in the polysaccharides distribution in the cell wall during apple fruit development and senescence. Planta. 243: 935–945.
30. Wellner N, Kacurakova M, Malovikova A, Wilson RH, Belton PS. 1998. FTIR study of pectate and pectinate gels formed by divalent cations. Carbohydr Res. 308:123–131.
31. Bichara LC, *et al.* 2016. Structural and spectroscopic study of a pectin isolated from citrus peel by using FTIR and FT-Raman spectra and DFT calculations. Infrared Phys Technol. 76: 315–327.
32. Debon SJJ, Tester RF. 2001. In-vitro binding of calcium, iron and zinc by non-starch polysaccharides. Food Chem. 73:401–410.
33. Jarvis MC, Apperley DC. 1995. Chain conformation in concentrated pectic gels: evidence from 13C NMR. Carbohydr Res. 275:131–145.
34. Gendensuren B, He C, Oh ES. 2020. Preparation of pectin-based dual-crosslinked network as a binder for high performance Si/C anode for LIBs. Korean J Chem Eng. 37:366–373.
35. Wang JT, Wan CC, Hong JL. 2020. Polymer blends of pectin/poly(acrylic acid) as efficient binders for silicon anodes in lithium-ion batteries. ChemElectroChem. 7:3106–3115.
36. Yourey W, Fu Y, Li N, Battaglia V, Tong W. 2019. Determining accelerated charging procedure from half cell characterization. J Electrochem Soc. 166:A1432.
37. Takahara I, Mizoguchi T. 2021. First principles study on formation and migration energies of sodium and lithium in graphite. Phys Rev Materials. 5:085401.
38. Sun B, *et al.* 2017. An organic nonvolatile resistive switching memory device fabricated with natural pectin from fruit peel. Org Electron. 42:181–186.
39. Cheong KY, Tayeb IA, Zhao F, Abdullah JM. 2021. Review on resistive switching mechanisms of bio-organic thin film for non-volatile memory applications. Nanotechnol Rev. 10:680–709.
40. Lim ZX, Cheong KY. 2018. Nonvolatile memory device based on bipolar and unipolar resistive switching in bio-organic aloe polysaccharides thin film. Adv Mater Technol. 3:1800007.
41. Jung SM, Kim DW, Jung HY. 2020. Unconventional capacity increase kinetics of a chemically engineered SnO_2 aerogel anode for long-term stable lithium-ion batteries. J Mater Chem A. 8:8244–8254.
42. Wang Y, *et al.* 2015. Designed hybrid nanostructure with catalytic effect: beyond the theoretical capacity of SnO_2 anode material for lithium-ion batteries. Sci Rep. 5:9164.
43. Cheng Y, *et al.* 2017. Adjusting the chemical bonding of SnO2@CNT composite for enhanced conversion reaction kinetics. Small. 13:1700656.
44. Arshad N, *et al.* 2021. Green thin film for stable electrical switching in a low-cost washable memory device: proof of concept. RSC Adv. 11:4327.
45. Hua B, *et al.* 2019. Understanding of pre-lithiation of poly(acrylic acid) binder: striking the balances between the cycling performance and slurry stability for silicon-graphite composite electrodes in Li-ion batteries. J Power Sources. 416:125–131.
46. Li S, *et al.* 2015. Surface capacitive contributions: towards high rate anode materials for sodium ion batteries. Nano Energy. 12:224–230.
47. Ciucci F, Chen C. 2015. Analysis of electrochemical impedance spectroscopy data using the distribution of relaxation times: a Bayesian and hierarchical Bayesian approach. Electrochim Acta. 167:439–454.
48. Wan TH, Saccocio M, Chen CF. 2015. Influence of the discretization methods on the distribution of relaxation times deconvolution: implementing radial basis functions with DRTtools. Electrochim Acta. 184:483–499.